Journal of Physics B: Atomic, Molecular and Optical Physics

PAPER • OPEN ACCESS

Time-resolved site-selective imaging of predissociation and charge transfer dynamics: the CH_3I B-band

To cite this article: Ruaridh Forbes *et al* 2020 *J. Phys. B: At. Mol. Opt. Phys.* **53** 224001

OPEN ACCESS
IOP Publishing
Journal of Physics B: Atomic, Molecular and Optical Physics
J. Phys. B: At. Mol. Opt. Phys. **53** (2020) 224001 (13pp)
https://doi.org/10.1088/1361-6455/abb1fd

Time-resolved site-selective imaging of predissociation and charge transfer dynamics: the CH_3I B-band

Ruaridh Forbes[1,8,*], **Felix Allum**[2,8], **Sadia Bari**[3], **Rebecca Boll**[4], **Kurtis Borne**[5], **Mark Brouard**[2], **Philip H Bucksbaum**[1], **Nagitha Ekanayake**[3], **Benjamin Erk**[3], **Andrew J Howard**[1], **Per Johnsson**[6], **Jason W L Lee**[3], **Bastian Manschwetus**[3], **Robert Mason**[2], **Christopher Passow**[3], **Jasper Peschel**[6], **Daniel E Rivas**[4], **Aljoscha Rörig**[4], **Arnaud Rouzée**[7], **Claire Vallance**[2], **Farzaneh Ziaee**[5], **Daniel Rolles**[5] and **Michael Burt**[2,*]

[1] Stanford PULSE Institute, SLAC National Accelerator Laboratory, 2575 Sand Hill Road, Menlo Park, CA 94025, United State of America
[2] Chemistry Research Laboratory, Department of Chemistry, University of Oxford, Oxford OX1 3TA, United Kingdom
[3] Deutsches Elektronen-Synchrotron (DESY), Notkestraße 85, 22607 Hamburg, Germany
[4] European XFEL, Holzkoppel 4, 22869 Schenefeld, Germany
[5] J. R. Macdonald Laboratory, Department of Physics, Kansas State University, Manhattan, Kansas 66506, United States of America
[6] Department of Physics, Lund University, 22100 Lund, Sweden
[7] Max-Born-Institute, Max-Born-Straße 2A, 12489 Berlin, Germany

E-mail: ruforbes@stanford.edu and michael.burt@chem.ox.ac.uk

Received 6 June 2020, revised 12 July 2020
Accepted for publication 24 August 2020
Published 22 October 2020

Abstract

The predissociation dynamics of the 6s (B^2E) Rydberg state of gas-phase CH_3I were investigated by time-resolved Coulomb-explosion imaging using extreme ultraviolet (XUV) free-electron laser pulses. Inner-shell ionization at the iodine 4d edge was utilized to provide a site-specific probe of the ensuing dynamics. The combination of a velocity-map imaging (VMI) spectrometer coupled with the pixel imaging mass spectrometry (PImMS) camera permitted three-dimensional ionic fragment momenta to be recorded simultaneously for a wide range of iodine charge states. In accord with previous studies, initial excitation at 201.2 nm results in internal conversion and subsequent dissociation on the lower-lying A-state surface on a picosecond time scale. Examination of the time-dependent yield of low kinetic energy iodine fragments yields mechanistic insights into the predissociation and subsequent charge transfer following multiple ionization of the iodine products. The effect of charge transfer was observed through differing delay-dependencies of the various iodine charge states, from which critical internuclear distances for charge transfer could be inferred and compared to a classical over-the-barrier model. Time-dependent photofragment angular anisotropy parameters were extracted from the central slice of the Newton sphere, without Abel inversion, and highlight the effect of rotation of the parent molecule before dissociation, as observed in previous

---

[8] These authors contributed equally to this work.
[*] Author to whom any correspondence should be addressed.

works. Our results demonstrate the ability to perform three-dimensional ion imaging at high event rates and showcase the potential benefits of this approach, particularly in relation to further time-resolved studies at free-electron laser facilities.

Keywords: photochemistry, time-resolved dynamics, ultrafast processes, free-electron laser science, velocity map imaging, photodissociation, charge transfer

(Some figures may appear in colour only in the online journal)

1. Introduction

Over several decades, methyl iodide (CH_3I) has served as the benchmark system for photodissociation dynamics in polyatomic molecules both experimentally and theoretically [1–7]. In particular, the C–I bond cleavage that arises from excitation of the first absorption band (A-band) constitutes one of the most studied processes in molecular photodissociation. The A-band absorption spectrum exhibits a broad structureless peak which gives rise to fast ballistic dissociation and results in population inversion between the spin–orbit excited, $I^*(^2P_{1/2})$, and ground, $I(^2P_{3/2})$, electronic states of the iodine atom [1, 2]. Initial time-resolved studies of this process focused on exploiting time-resolved mass spectrometry (TRMS) to characterize the product formation reaction times [8]. Later work examined the internal energy of the CH_3 fragment as well as spin–orbit branching ratios using resonantly enhanced multiphoton ionization (REMPI) [5] and served as a means to benchmark multidimensional wavepacket dynamic simulations [6, 7]. Recently, numerous experimental groups have explored inner-shell excitation or ionization at the iodine atomic site to track the ensuing photodissociation dynamics following A-band excitation using both free-electron lasers (FELs) [9–12] and high harmonic generation sources [13, 14]. Iodine-containing hydrocarbons are an exemplary choice for performing extreme ultraviolet (XUV) time-resolved studies due to the I $4d_{5/2,3/2} \rightarrow \epsilon f$ shape resonances (60–140 eV) [15, 16], which result in the photoabsorption being dominated by the I atom and, thus, the ability to excite or probe site-selectively.

The second absorption band (B-band) of CH_3I accesses the lowest-lying Rydberg state, which has a more complex photodissociation mechanism and has been the subject of fewer experimental studies. The B-band is comprised of transitions due to excitation of the non-bonding iodine 5p electrons to a 6s molecular Rydberg state [17]. Strong spin–orbit coupling of the resulting ionic ground state results in two states labelled $^2\Pi_{3/2}$ and $^2\Pi_{1/2}$ in $C_{\infty v}$ and $^2E_{1/2}$ and $^2E_{3/2}$ in C_{3v} symmetry, respectively. Transitions correlated with the lower-lying $^2E_{3/2}$ ionic core from the molecular ground state are located between 195 and 205 nm and, due to their C_{3v} symmetry, have a dipole moment perpendicular to the C–I bond [18]. Spectrally these excitations are characterized by a series of intense sharp peaks with the dominant component being the band origin (0^0_0) at 201.2 nm, which is the subject of this study.

Despite the B-band displaying a clear vibrational structure [17], the transitions exhibit significant spectral broadening due to finite lifetimes and the underlying predissociation mechanism. Predissociation occurs via interaction of the 6s orbital with some of the dissociative components of the A-band. *Ab initio* calculations by Alekseyev and coworkers highlight that the B-band E symmetry components can predissociate due to crossing with the repulsive 4E ($^3A_1$) valence state [3, 4], which asymptotically correlates with the $I^*(^2P_{1/2}) + CH_3$ dissociation limit. A diagram of the electronic states relevant to the present study is shown in figure 1.

The first direct measurements of the predissociation lifetime of the B-band were performed by Baronavski and Owrutsky using TRMS. A lifetime of 1.38 ± 0.14 ps was reported for the 0^0_0 origin band [19], however, the authors noted shorter lifetimes for higher vibrational levels [20]. Bañares *et al* presented a series of measurements on B-state predissociation, where time-resolved ion velocity map imaging (VMI) was utilized to provide detailed insight into the reaction mechanism [21–23]. These studies served to corroborate the early TRMS work, reporting a predissociation lifetime of 1.5 ± 0.1 ps, and also investigated directly the angular nature of the transition as well as the vibrational activity in the CH_3 radical [21]. Specifically, the angular distribution of the $I^*(^2P_{1/2})$ fragment, detected using REMPI, exhibits a time-dependent anisotropy, with β parameter values varying from $\beta \approx -0.9$ within the first picosecond to $\beta \approx -0.5$ at later pump–probe time-delays [21]. Similar measurements performed by Thiré *et al* reported $I^*(^2P_{1/2})$ β values of -0.549 ± 0.005 [24] at long pump–probe time-delays. Photofragment VMI studies have also reported predissociation lifetimes for the 2^1_0 and 3^1_0 vibronic levels, 0.85 ± 0.04 ps and 4.34 ± 0.13 ps, respectively, which highlights the strong sensitivity to the exact excitation wavelength [23]. Excitation of the 3^1_0 vibronic state also resulted in the first direct observation of ground state $I(^2P_{3/2})$ dissociation products [22], which had not previously been observed at the band origin [21, 24]. Recently, Xu and Pratt utilized a universal probing scheme at 118 nm to determine the branching into the $I^*(^2P_{1/2})$ and $I(^2P_{3/2})$ channels for specific vibronic states in the 6s $^2E_{3/2}$ manifold [25]. The study concluded that most excited vibronic states correlate with a small, but nonzero, branching ratio into the ground $I(^2P_{3/2})$ state. To the best of our knowledge, no investigations into the B-band predissociation mechanism exploiting inner-shell excitation or ionization as the probing mechanism have been performed to date, and therefore this constitutes a major focus in this present study.

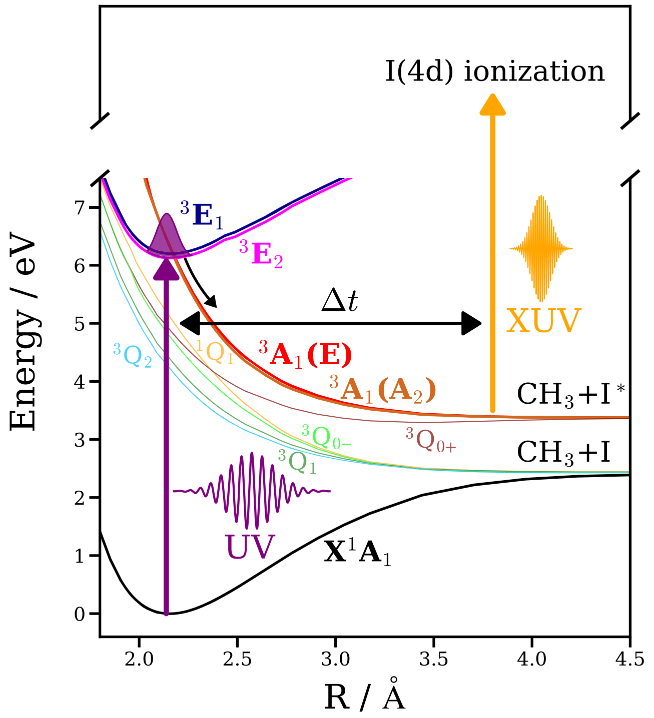

Figure 1. The theoretical potential energy curves of methyl iodide along the C–I stretching coordinate [4]. The electronic states relevant for this study are shown in bold. Excitation by the 201.2 nm pump pulse populates the onset of the B-band ($^3E_1/^3E_2$ Rydberg states). Non-adiabatic coupling results in population transfer to a lower-lying dissociative state and correlates with production of $CH_3 + I^*(^2P_{1/2})$. The ensuing dynamics are captured at variable pump–probe time-delay Δt by (multi-) photon ionization above the I 4d edge using an intense XUV FEL pulse.

In the present work, the predissociation mechanism following excitation into the 6s $(^2E_{3/2})$ 0_0^0 Rydberg state is investigated by inner-shell ionization. The dissociation process was followed using site-selective (multi-) photon absorption in an intense XUV FEL pulse, by recording the resulting charged fragments using VMI. We exploit the multimass capabilities of the pixel imaging mass spectrometry (PImMS) camera [26, 27] to simultaneously measure the three-dimensional ion momenta of multiply charged atomic I as a function of laser-FEL time-delay. Observed is the production of low kinetic energy (KE) fragments on a picosecond time scale, which is consistent with the predissociation mechanism of the 6s $(^2E_{3/2})$ band origin. Predissociation lifetimes of ∼1.55 ps are extracted from fits of the I^{n+} low KE ion-yield, which is found, within the experimental error, to be independent of iodine charge state. Time-resolved photoion angular distributions reveal the highly parallel nature of the B-band excitation, as well as a loss of anisotropy resulting from rotation of the parent molecules on a similar time scale to the predissociation. Closer examination of the delay-dependent, energy-resolved ion yields for differing iodine charge states reveals systematic shifts arising from electron transfer from the neutral methyl fragment to the highly charged iodine following multiple ionization by the XUV pulse, in keeping with previous studies [9, 11, 12]. A weak, high kinetic energy feature is also observed shortly after time-zero (t_0), and assigned to Coulomb explosion following charge transfer between nascent dissociation products. Analysis of these signatures of charge transfer allowed direct probing of the dependence of the charge transfer on internuclear distance and iodine charge state, which appear to be consistent with the classical over-the-barrier model [28], within experimental temporal resolution.

2. Experimental methods

The experiments were conducted using the CAMP@FLASH instrument [29] on beamline BL1 at the free-electron laser in Hamburg (FLASH) [30]. The setup comprises a double-sided VMI spectrometer capable of simultaneously measuring ions and electrons [29]. Commercially available CH_3I (>99% Sigma Aldrich) was expanded, after several freeze-pump-thaw cycles, into the CAMP chamber via two skimmers using a continuous jet without using a carrier gas. A liquid reservoir held at room temperature was directly connected to the gas delivery system for this purpose. The skimmed molecular beam was intersected at 90° by both the FLASH beam and the pump–probe laser.

The FLASH pump–probe laser system consists of a Ti:sapphire oscillator and a 10 Hz chirped pulse multipass amplifier (Coherent Inc., Hydra) capable of producing 12 mJ 55 fs pulses at a central wavelength of 810 nm [31]. An 8 mJ fraction of the total laser output was used for these experiments. The beam passed through a 50:50 beamsplitter to provide beams for a subsequent nonlinear mixing scheme. The reflected component was frequency tripled using a pair of β-BaB_2O_4 (BBO) crystals and the resultant third harmonic separated from the fundamental and second harmonic beams using a series of dichroic mirrors. The transmitted component was further split by a 50:50 beamsplitter to provide beams for cross correlation measurements and additional nonlinear mixing. The latter of these was recombined and overlapped spatially as well as temporally with the third harmonic pulse in a BBO crystal to provide the fourth harmonic of the FLASH pump–probe laser via sum-frequency generation. A series of dichroic mirrors were utilized to separate the residual third harmonic and fundamental light from the fourth harmonic beam. The fourth harmonic central wavelength was selected to coincide with the 6s $(^2E_{3/2})$ 0_0^0 Rydberg state of CH_3I at 201.2 nm [17], via tuning of the phase matching angle of the final BBO crystal. It had a bandwidth of 0.75 nm. Typical pulse energies for the 201.2 nm light during the experiment were ∼0.5–1 μJ, and these were adjusted to minimize contributions associated with two-photon ionization of the molecular ground state.

The pulse duration of the ultraviolet (UV) pump pulse was characterized *in situ* by performing non-resonant two-color multiphoton ionization of Xe with the fourth harmonic and the fundamental of the FLASH pump–probe laser system. Figure 2 shows the time-resolved ion-yield for Xe^+ as a function of UV + infrared (IR) pump–probe time-delay. Fitting this transient feature to a Gaussian function yields a cross-correlation width, τ_{xcorr}, of 141 ± 6 fs. Based on the literature ionization potential of 12.1298 eV, a total of 4 IR

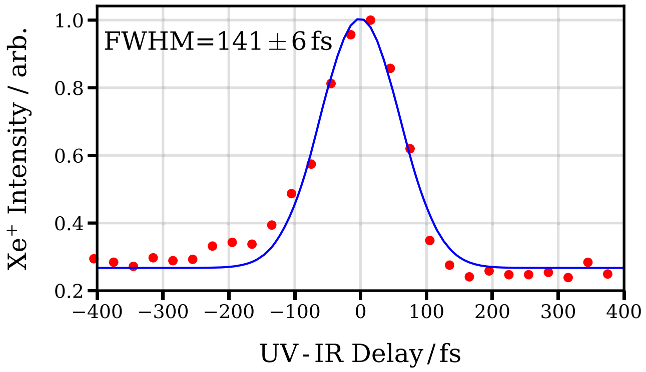

Figure 2. Cross-correlation trace of the fundamental and fourth harmonic of the FLASH pump–probe laser system measured via two-color multiphoton ionization in Xe using PImMS. A Gaussian fit to the time-dependent Xe^+ signal yields a full width at half maximum of 141 ± 6 fs, where the error represents the standard error on the fitted parameter.

photons are required to create Xe^+ (i.e. a 201.2 nm + 4 × 810 nm ionization process) and a lower limit of the pulse duration can be estimated using $\tau^2_{\mathrm{xcorr}} = \tau^2_{810\mathrm{nm}}/4 + \tau^2_{201.2\mathrm{nm}}$, where $\tau_{810\mathrm{nm}}$ and $\tau_{201.2\mathrm{nm}}$ represent the duration of the 810 nm and 201.2 nm pulses, respectively. Independent measurements of $\tau_{810\mathrm{nm}}$ were performed using an autocorrelator ($\tau_{810\mathrm{nm}} = 57 \pm 3$ fs) and a value of $\tau_{201.2\mathrm{nm}} = 138 \pm 3$ fs could be determined. The extracted value is significantly longer than the Fourier-transform-limited pulse duration, assuming a Gaussian pulse shape, of 80 fs based on the measured spectral bandwidth. This discrepancy is expected due to dispersion from propagation of the UV pulse through the 5 mm $\mathrm{CaF_2}$ entrance window on the CAMP instrument as well as propagation in the BBO crystals. For the employed pulse energies and assuming a focal spot size diameter of 30 μm, based on Gaussian beam optics, an upper limit of low 10^{12} W cm^{-2} was obtained for the UV intensity. The temporal overlap between the UV and FEL pulse was determined *in situ* using the following method. Initially, the overlap between the IR and FEL pulses was found by monitoring the ratio of $\mathrm{Xe}^{2+}/\mathrm{Xe}^{3+}$ in a two-color experiment. This ratio decreases when the FEL preceeds the IR pulse, due to the IR pulse post-ionizing metastable Xe^{2+} ions formed following Xe (4d) ionization and Auger decay [32–34]. Fitting this ratio as a function of delay to a normal cumulative distribution function yielded t_0 between the IR and FEL. Combining this with the UV/IR t_0 allowed the UV/FEL t_0 to be determined. This procedure was carried out prior to the acquisition of the $\mathrm{CH_3I}$ data, and although relative timing of the optical laser and the FEL appeared stable during the experiments, there is some uncertainty in the precise value of t_0 due to possible experimental drift.

A holey mirror was utilized for laser incoupling to achieve nearly co-propagating UV and FEL pulses. The polarization directions of pump and probe light were parallel to each other in the detection plane, permitting the use of standard Abel inversion techniques [35]. A computer-controlled delay stage in the fundamental beampath before nonlinear mixing provided a variable time between the laser-pump and FEL-probe pulses. The central wavelength of the intense XUV FEL pulse was selected to coincide with the maximum of the I 4d$_{5/2,3/2}$ → ϵf shape resonances [15, 16] (95 eV), ensuring site-specific probing at the iodine atom. Due to the high absorption cross section at the shape resonance, an FEL pulse energy of approximately 1 μJ was utilized. However, to ensure reasonable pulse-to-pulse stability, the FEL was operated under higher gain conditions and then filtered to the desired pulse energy by a series of thin Zr and Nb filters. Pulse energies of 25 ± 6.4 μJ were recorded using an upstream gas monitor detector (GMD), and the FEL pulse duration was estimated to be 50–60 fs [36]. Based on previous measurements [29] and an assumed FEL focal spot size of 10 μm, this corresponds to approximately 10^{13} W cm^{-2} for the XUV intensity.

Ions created from the interaction of the FEL with $\mathrm{CH_3I}$ were recorded using a VMI spectrometer equipped with two microchannel plates (MCPs) coupled to a P47 phosphor screen. The electrostatic optics were operated under conditions such that ions with the same initial transverse velocity, relative to the time-of-flight (ToF) axis, and mass-to-charge ratio (m/z) arrive at the same position on the MCP [37]. Flashes on the phosphor screen were imaged by the PImMS camera [26, 27], equipped with a PImMS2 sensor. The sensor is a 324 × 324 pixel detector that recorded the spatial positions (x, y) as well as arrival times (t) of incident photons with a precision of 25 ns and with time-stamping of up to four ion hits per pixel per trigger/readout (10 Hz). This provides a means to record all ionic fragments within a given laser shot at a resolution sufficient to differentiate most ion fragments for our employed ion optic voltages. Furthermore, recording all ion momenta in a single laser shot permits data to be collected under conditions suitable for covariance or coincidence imaging and hence correlations to be extracted for different fragmentation channels [38, 39].

Centroiding of the observed (x, y, t) ion data was performed, due to each ion hit generally spanning multiple pixels and time bin registers, to improve the achievable three-dimensional momentum resolution [40]. Calibration of the mass-to-charge ratio was performed using the distributions of different iodine charge states and cross-checked using atomic Xe under the same voltage conditions. The transverse momentum calibration (i.e. pixel to kinetic energy) was performed using ion trajectory simulations, carried out using the SIMION 8.1 software package [41], from which an empirical formula for the relationship between the hit position and fragment kinetic energy was constructed. Fluctuations in the FEL pulse energy and timing were monitored on a shot-to-shot basis [42], using the measurements of the gas monitor detector [43] and the bunch arrival monitor (BAM) [44], respectively.

3. Results and discussion

Figure 3 shows the averaged mass spectra for the ionization of $\mathrm{CH_3I}$ by the UV pulse and the XUV pulse separately, as well as by both pulses at positive pump–probe delays (UV preceding the FEL). The dominant pump–probe channel of interest in the present work is single-photon UV excitation to the B-state in $\mathrm{CH_3I}$, hence to limit unwanted contributions due to multiphoton ionization, the intensity of the 201.2 nm pulse was

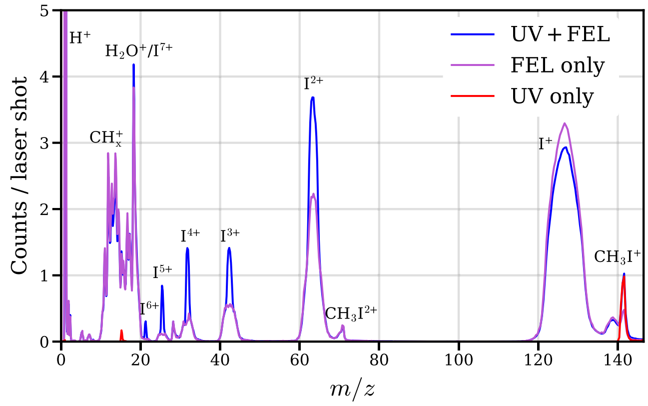

Figure 3. Centroided CH_3I mass spectra recorded by PImMS for UV + FEL (blue), FEL only (purple) and UV only (red). Each spectrum was normalized by the total number of shots. The UV + FEL data was summed over all positive pump–probe time-delays corresponding to the UV preceding the FEL pulse.

set to barely ionize the molecular ground state. This is reflected in the UV only mass spectrum where the CH_3I^+ parent ion as well as small amounts of CH_3^+ fragment were observed. Favorable production of the parent ion is in accord with the expectation that the 6s $^2E_{3/2}$ Rydberg state correlates well with the ionic core of the CH_3I^+ ground state [17].

The interaction of the parent molecules with the FEL pulse alone predominantly results in production of charged atomic iodine up to I^{6+} paired with CH_x^+ (with $x \leqslant 3$), as well as singly- and multiply-charged carbon ions. The ion spectra also contain a significant amount of H_2O^+ and its fragments stemming from the ionization of residual gas. The presence of iodine charge states beyond I^{3+} is a clear indication of multiphoton ionization initiated by the FEL pulse. Comparison with synchrotron measurements of single-photon ionization of Xe, which is isoelectronic with I^- and likely has similar ionization cross sections as well as Auger decay pathways, at our employed photon energy of 95 eV suggests that only charge states lower than Xe^{3+} are formed in the single-photon process [45]. Identification of charge states of I^{n+} with $n > 6$ is hampered by overlapping ToF features with H_2O^+ and CH_x^+, and the limited temporal resolution of the PImMS camera. These higher charge states are, however, likely present in the current experiment, given the employed FEL intensity.

Two distinct classes of pump–probe features are observed in the mass spectrum, namely: (i) enhancement in the yield of multiply charged atomic iodine (I^{2+} to I^{6+}), and (ii) depletion of I^+ yield and the yield of numerous fragments between $m/z = 10$ to 15. The former results in a slight narrowing of the I^{2-6+} peaks, compared to the FEL only case, which can be attributed to low KE atomic iodine fragments produced via neutral dissociation, as in several previous studies [9, 11, 12]. The presence of low KE iodine fragments is more clearly observed in the sliced velocity map images associated with a particular 25 ns time bin. Figure 4 shows images of the transverse velocities for various iodine fragments for the central 1–2 time bins of a given ToF peak. For each ion, UV late and UV early data are shown in the left- and right-hand side of the images, respectively. Focusing initially on the I^{2+} fragment, it is evident that two distinct features are observed: an intense feature at relatively low radii observed only after time-zero, and a weaker diffuse feature at larger radii. The former of these relates to ionization of neutral atomic iodine produced via the predissociation process, whereas the latter is connected with the Coulomb explosion of neutral parent molecule by the FEL pulse. Features due to the same processes are also present in the higher iodine charge state images but with significantly reduced relative intensity in the Coulomb explosion channel. The pump–probe feature associated with neutral predissociation is observed at lower radii for higher charge states–this is to be expected as under VMI conditions, radius is proportional to $1/\sqrt{q}$, for an ion of charge q [37]. We note that the photoion angular distribution associated with the production of neutral iodine via predissociation is peaked perpendicularly to the laser polarization axis, defined vertically in figure 4. Previous studies reported qualitatively similar photofragment anisotropies, as discussed in more detail in section 3.3.

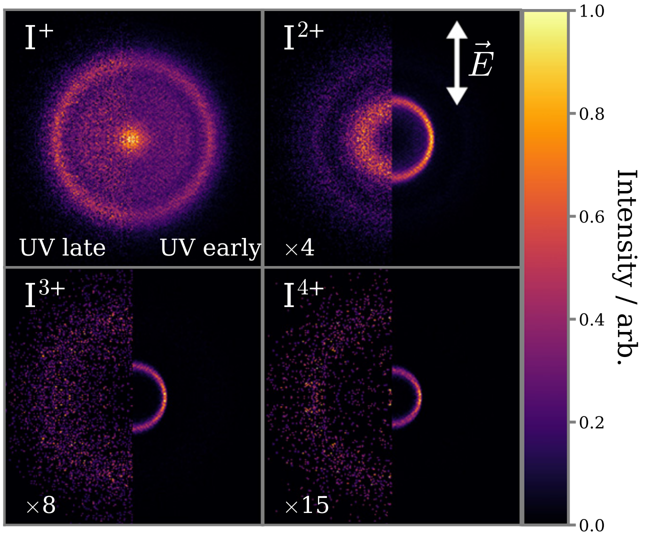

Figure 4. Sliced ion images for the I^+ to I^{4+} fragments for a specific 25 ns time bin(s) corresponding to the centre of the ToF peak. These images are generated from the centroided ion hits and have also undergone four-fold symmetrization about the laser polarization axis, $\vec{E}$. For each ion, the left-hand side of the image corresponds to negative pump–probe delays (UV late), while the right-hand side corresponds to positive pump–probe delays (UV early). For I^{2+} to I^{4+}, the UV late data has been multiplied in intensity by the displayed factor, to increase the visibility of the weak features.

3.1. Three-dimensional ion imaging

In conventional VMI experiments, the recorded velocity distributions are two-dimensional projections of the Newton sphere, as a result of 'crushing' in the plane of the detector [37]. In systems with cylindrical symmetry, such as the present experiment (along the polarization vector of the UV and XUV pulses), a cut through the three-dimensional distribution may be extracted by applying the inverse Abel transform [46], for which several numerical methods have been developed [35, 47–51]. Alternatively, these transformation methods (and the inherent addition of noise) may be avoided by gating the detector in time such that only the 'central slice' of the Newton sphere of velocities is recorded, corresponding to ions with minimal velocity along the laboratory ToF axis. The radial and angular dependence of the original three-dimensional velocity distribution can then be extracted from this central slice, assuming cylindrical symmetry. Multiple experimental schemes have been developed to carry out high-resolution slice imaging, generally by modifying ion optics potentials in order to temporally stretch ion Newton spheres, allowing a thin central slice to be imaged [52–54]. Particularly in the context of time-restricted experiments at external user facilities, such as FLASH, this methodology has one major disadvantage. By only imaging the central slice of the velocity distributions, relatively few ion events can be recorded, increasing the experimental time required to acquire a meaningful velocity distribution. Further improving the slicing resolution (i.e. imaging thinner slices) only exacerbates this problem, as does extending the approach to time-resolved studies. The intuitive solution to this is to record the ion data in a fully three-dimensional manner, allowing all the ion events to be usefully analyzed, while still avoiding the inverse Abel transform. At low count rates, this can be achieved with very high resolution using a cold target recoil ion momentum spectrometer (COLTRIMS) or reaction microscope [55, 56]. Due to the rather low repetition rate of many current FELs (10 to 120 Hz), operation at a far higher count rate is often desirable. At these count rates (approximately 65 ions per shot in the current experiment, for example), three-dimensional imaging can be achieved by coupling a VMI spectrometer with a fast time-stamping detector, such as the PImMS camera [27] or TimepixCam [57, 58]. Instead of a single time-sliced image through the central slice of the Newton sphere, many time-sliced images through the Newton sphere may be recorded [59, 60], with each time-sliced image corresponding to different initial ion velocities along the ToF axis. In the present experiment, sufficient stretching of the ion ToF peaks to allow many time-sliced images to be recorded was achieved by employing low ion optics voltages. Figure 5(a) shows example time-sliced images for the I^{2+} ion, plotted for all positive pump–probe delays. Each image corresponds to a different 25 ns PImMS time bin and thus a different range of ion velocities along the ToF axis, as depicted in figure 5(b).

Using ion trajectory simulations of the spectrometer, in SIMION [41], ion events in terms of position (x, y) and arrival time (t) at the detector can be calibrated into initial ion velocities along the lab-frame X, Y and ToF axes, respectively. From these, a total velocity, v for each ion event can be calculated as $v = \sqrt{v_X{}^2 + v_Y{}^2 + v_{\mathrm{ToF}}^2}$. An example velocity distribution calculated this way is plotted in blue in figure 5(c) for a single 100 fs pump–probe delay bin, comprising *ca.* 600 laser shots and 6000 I^{2+} ion events. For comparison, velocity distributions obtained using only the central slice ion images (red) or through Abel inversion of the crushed ion images (i.e. summed images across the entire I^{2+} ToF range) using the pBASEX algorithm (purple) [35, 61]. It can be seen that the three-dimensional analysis of the data yields a velocity distribution with a significantly improved signal-to-noise ratio, as all the recorded data can be usefully analyzed. This improvement in data quality was crucial for the detailed pump–probe time-resolved analysis presented in sections 3.2 and 3.3. Additionally, cylindrical symmetry is no longer required to extract velocity information, facilitating future experiments with more complex pump and probe polarization geometries. Higher resolution time-stamped detection (e.g., using Tpx3cam [62]) would also improve the achievable three-dimensional velocity resolution. As such, our results lead us to conclude that 3D imaging will be a powerful tool in future time-resolved FEL studies, especially considering the continual technological advancements in fast time-stamping detectors [58, 62].

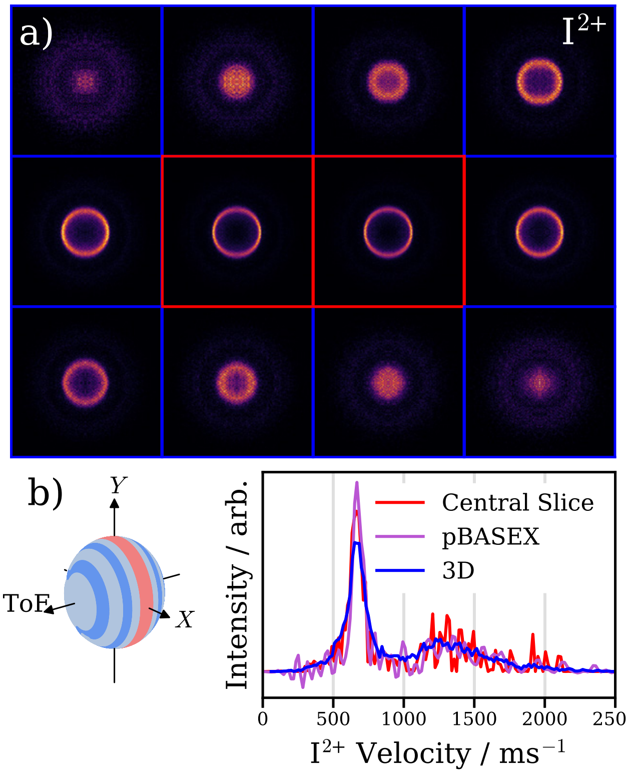

Figure 5. (a) Series of example time-sliced images of the I^{2+} ion. Each image corresponds to a single 25 ns PImMS time bin, and the data has been summed over all positive (UV early) pump–probe delays. (b) Schematic illustration of three-dimensional time-slicing of a Newton sphere. Successive time-sliced images are shaded in different colors, with the central slices shaded red. (c) Example I^{2+} velocity distributions obtained for a single pump–probe delay bin, by analyzing only the central slice (red), through Abel inversion of the two-dimensional crushed ion image (purple) or analyzing the data in three dimensions, as described in the text (blue).

3.2. *Photofragment kinetic energies and transient yields*

The time-dependencies of the iodine fragment momenta shown in figure 4 are more clearly visualized by plotting time-dependent kinetic energies. The kinetic energy distribution of the I^{2+} fragment is shown in figure 6(a) alongside the integrated transient for the low-kinetic energy, delay-dependent feature in panel (b). These KE distributions are generated by performing integration over both the polar

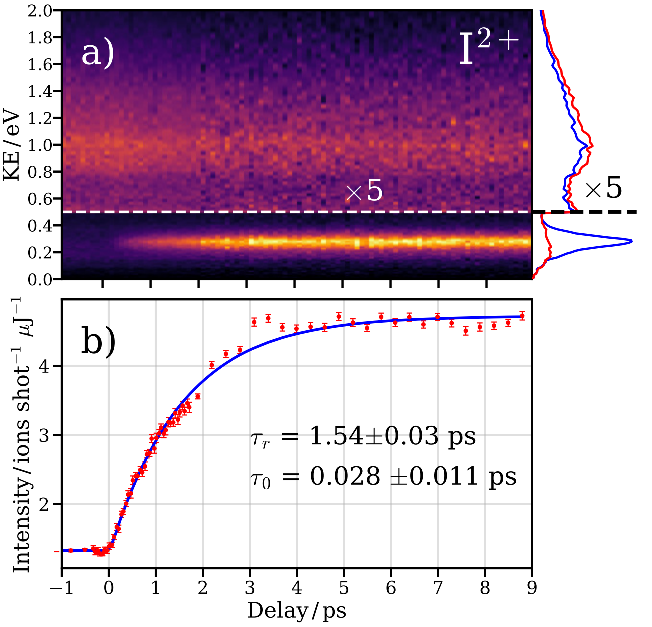

Figure 6. (a) The time-resolved I^{2+} KE distribution obtained from integration of the polar and azimuthal angles of the 3D Newton sphere (as detailed in section 3.1). Negative delays correspond to the FEL probe pulse arriving before the UV pump pulses, and vice versa. Above 0.5 eV, intensities have been scaled by a factor of 5 in order to more clearly show the depletion of the broad, high KE feature. Kinetic energy distributions for UV late (−1 ps to 0 ps) and UV early (+8 ps to +9 ps) pump–probe delays are projected in red and blue, respectively. (b) Integrated ion yields for the low kinetic energy feature (∼0.2–0.4 eV), fit using the model described in the text. The extracted fit parameters for I^{2+}, as well as higher charge states are provided in table 1. Note, the displayed error bars correspond to the statistical counting error.

and azimuthal angles, thereby utilizing the 3D momentum imaging capabilities of the PImMS camera, as well as normalizing by the number of frames and by the FEL pulse energy, recorded on a shot-to-shot basis. Images were recorded over a pump–probe time-delay range spanning approximately −1 to 9 ps with variable step size but re-sorted to smaller steps, based on the BAM measurements [42].

The transient yield for the low KE region highlights the monotonically increasing behavior of the I^{2+} fragments (see figure 6 panel (b)). The low KE channel can be assigned to C–I bond cleavage of the neutral molecule and production of a neutral iodine atom, which is subsequently ionized by the FEL pulse [9, 11, 12]. This is corroborated by the narrow KE distribution of the associated I^{2+} since the methyl cofragment likely remains neutral due to its much weaker soft x-ray absorption cross section. This is in stark contrast to ionization induced dissociation (i.e. where one fragment is charged before interaction with the FEL pulse), which results in time-dependent KEs, due to the Coulomb repulsion changing as a function of internuclear distance [11]. Time-dependent KEs were also previously observed in our work probing photodissociation dynamics using near-infrared Coulomb explosion imaging, where the ionizing laser field, unlike the FEL at this wavelength, interacts with both neutral fragments [39, 63, 64].

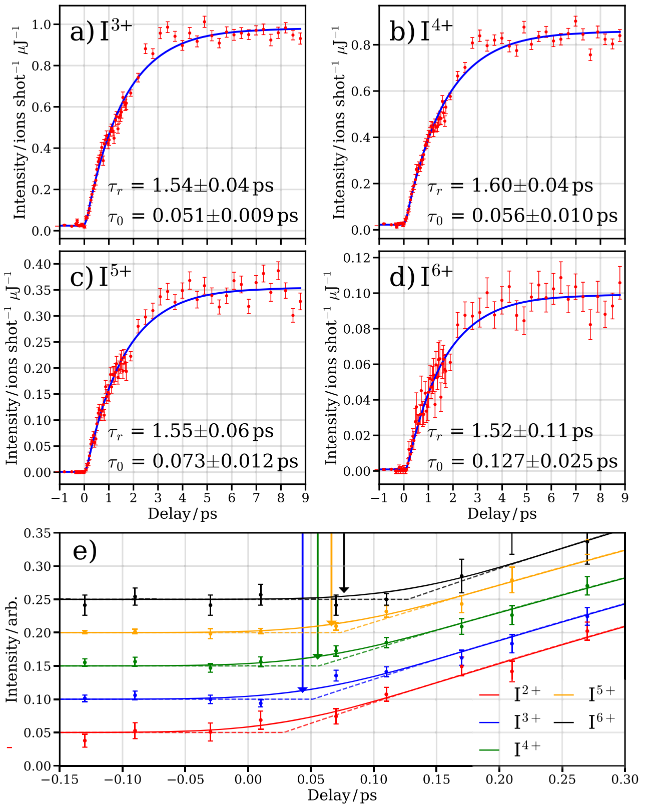

Figure 7. Time-resolved yields of the low KE (∼0.2–0.4 eV) ions for (a) I^{3+}, (b) I^{4+}, (c) I^{5+} and (d) I^{6+}. Experimental data with statistical error bars are shown in red, while fits using the function shown in the text are plotted in blue. The exponential rise time, τ_r, and time offset, τ_0, for each fit are overlaid. Panel (e) displays time-resolved yields of low KE I^{2+} to I^{6+} ions shortly after time-zero. Fits for each ion are plotted both with (solid lines) and without (dashed lines) Gaussian convolution by the instrument response function. Offset times predicted by the over-the-barrier model, relative to the fitted offset time for I^{2+} are displayed for each ion as colored arrows.

In order to model the time-dependence of the low KE transient, a fitting function employing the product of an exponential rise and a Heaviside step function convoluted with a Gaussian instrument response function was used. Fits to the experimental data (see figure 6(b)) yield two quantities: (i) the time offset, τ_0, of the rising component from the temporal overlap of the UV and FEL pulses; and (ii) the rise time, τ_r of the exponential. The temporal instrument response can be estimated from the lower limit of $\tau_{201.2\mathrm{nm}}$ determined in section 2 and the estimated FEL pulse duration of 50 fs. This yields a value of 147 fs, which was used in the fitting. An offset between the temporal overlap and appearance of the iodine fragment is expected, due to the time associated with wavepacket motion on the dissociative state, and was determined to be 28 ± 11 fs for the I^{2+} channel. The fit extracts a transient rise time of 1.54 ± 0.03 ps, which is in excellent agreement with previous studies [19, 21, 24]. Analysis of the low KE feature in I^{3+}–I^{6+} confirms that the agreement of the rise time extends to higher iodine charge states but also highlights a statistically significant discrepancy in the onset time as a function of charge state (see figure 7). This discrepancy can be related, similarly to our previous work [9, 11, 12], to a

Table 1. Extracted parameters from fits of the low kinetic energy I^{n+} ions ($n = 2$–6). The final column shows the relative time offsets predicted by the over-the-barrier model, as described in the text.

Ion	τ_r/ps	τ_0/fs	$\tau_0 - \tau_0(I^{2+})$/fs	$\tau_{crit} - \tau_{crit}(I^{2+})$/fs
I^{2+}	1.54 ± 0.03	28 ± 11	—	—
I^{3+}	1.54 ± 0.04	51 ± 9	23 ± 14	15
I^{4+}	1.60 ± 0.04	56 ± 10	28 ± 15	27
I^{5+}	1.55 ± 0.06	73 ± 12	45 ± 16	38
I^{6+}	1.52 ± 0.11	127 ± 25	99 ± 27	48

charge transfer process, which will be discussed in section 3.2. A summary of fit parameters for the low KE feature in I^{2+}–I^{6+} is given in table 1.

The asymptotic value of the KE, 0.30 eV, for low energy I^{2+}, is in accord with the previous work of Gitzinger *et al*, where iodine atom center of mass kinetic energies of approximately 0.29 eV were reported [21]. Our measured KE can be compared to the maximum available KE, KE_{max}, for the $I^*(^2P_{1/2}) + CH_3$ dissociation channel, calculated via $KE_{max} = (m_{CH3}/m_{CH3I}) \times (h\nu_{201.2nm} - D_0 - E_{SO})$, assuming that the CH_3 radical carries negligible internal energy. Here, m_{CH3} and m_{CH3I} refer to the mass of CH_3 and CH_3I, respectively, $h\nu_{201.2nm}$ refers to pump photon energy, D_0 is the C–I bond dissociation energy and E_{SO} is the spin–orbit splitting of atomic iodine. A KE_{max} of 0.297 eV is extracted from this estimation, which, given the excellent agreement with our measured KE, suggests only a small amount of internal energy release into the CH_3 cofragment during dissociation. This is in keeping with previous studies [21], where only a few quanta of the ν_1 and ν_2 vibrational modes in the CH_3 fragment were populated during B-band predissociation. A similar calculation performed for the $I(^2P_{3/2}) + CH_3$ dissociation results in a KE_{max} of 1.233 eV, confirming the absence of this channel, in accord with previous time-resolved results for the 0_0^0 vibronic state of the B-band [21, 24]. A recent detailed investigation of the vibrational level dependence, in the initial excitation, on the photodissociation branching ratio highlighted a 0.01 ± 0.01 quantum yield for the $I(^2P_{3/2}) + CH_3$ channel [25]. Finally, we note that asymptotic values of approximately 0.3 eV were also extracted for the momenta associated with higher iodine charge states (I^{3+} to I^{6+}).

3.3. Charge transfer signatures

The intense XUV pulse used in the present study may initiate multiple photoionizations and Auger decays at the iodine atom, leading to a highly localized positive charge. In a molecular environment, this charge is rapidly redistributed and leads to a Coulomb explosion. This results in the production of ions such as CH_x^+ ($x = 0, 1, 2, 3$) and H^+ in high yield following irradiation with the FEL pulse alone (figure 3) as well as the high kinetic energy channels observed in I^{n+} arising from Coulomb explosion. If the C–I bond dissociates prior to multiple ionization by the FEL pulse, charge may still transfer to the neutral CH_3 cofragment, but the probability for this depends strongly on fragment separation. In the limit of sufficiently large internuclear distances, charge transfer no longer occurs. This behaviour in CH_3I was observed by Erk *et al* [9], who employed intense 800 nm pump and 1500 eV probe pulses. The near-infrared pulse predominantly induced dissociative ionization, while the XUV pulse multiply ionized the molecule selectively via the iodine *M* shell. Monitoring the delay-dependent rise of the low kinetic energy feature (arising from dissociative ionization followed by multiple inner-shell ionization) in a range of iodine charge states revealed a shift to later onset times, which increased with charge state. This was interpreted as an increase in the critical internuclear distance at which charge transfer is no longer possible for increasing iodine charge state. At shorter pump–probe delays and thus shorter internuclear distances, charge is transferred, and the ions repel and are produced with higher KEs. These results (and results from follow-up experiments [11, 12]) could be understood within the theoretical framework of a classical over-the-barrier model, originally developed for ion–atom collisions [28]. Here, charge may be only transferred if the Coulombic barrier to electron transfer is lower than the ionization energy of the site 'donating' the electron. As this barrier rises with internuclear distance, a critical separation, r_{crit}, may be derived, beyond which charge transfer is forbidden. For the case of electron transfer from iodine with charge n to a neutral CH_3, r_{crit} is given in atomic units by [9]:

$$r_{crit}(n) = \frac{1 + 2\sqrt{n}}{IP_{CH_3}} \tag{1}$$

where IP_{CH_3} is the ionization energy of the methyl radical.

In the present study, the predissociation dynamics induced by the 201.2 nm pump pulse is rather different to the dissociative ionization or direct neutral dissociation used in our previous studies [9, 11, 12] employing 800 nm and 270 nm light, respectively. However, the physics of the subsequent charge transfer processes are unchanged, and once more a shift in the onset of the low KE ions for increasing iodine charge state is to be expected. Fits of the low KE I^{n+}, ions, as described in detail for the I^{2+} ion in section 3.1, are shown in figure 7 for $n = 3$–6 in panels (a)–(d).

A shift in the exponential rise in the ion yield can be clearly observed, with the start of the exponential rise systematically moving to later delays for higher iodine charge states, where a greater r_{crit} is expected. To make a quantitative comparison to the over-the-barrier model, it is helpful to view these τ_0 values relative to that of I^{2+}, which removes any ambiguity about the precise assignment of the t_0 of the experiment. These values may then be compared with shifts predicted by the over-the-barrier model, relative to the I^{2+} ion, assuming a constant relative velocity between the CH_3 and I fragments following dissociation. The measured, and reference [21], KE of approximately 0.29 eV for the iodine fragment corresponds to a relative velocity of 63 Å ps^{-1}. Assuming this recoil velocity is reached instantaneously at the time of ionization gives the predicted time delay shifts plotted as colored arrows in figure 7(e) and shown in the fifth column of table 1. The agreement observed is generally very good, despite limitations such as the temporal resolution of the experiment and the simplicity of the model. The I^{6+} ion shows a relatively poor agreement with the model, exhibiting a significantly greater shift in

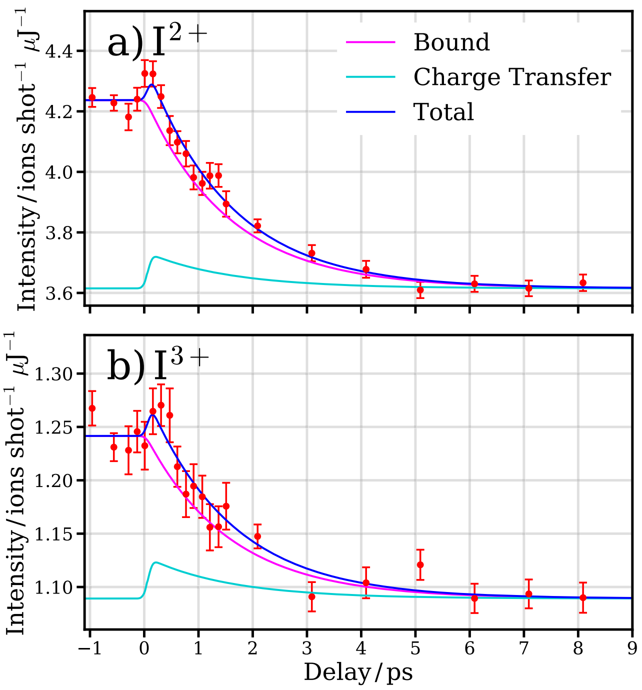

Figure 8. Time-resolved yields of the high KE ions for (a) I^{2+} and (b) I^{3+}. Experimental data with statistical error bars are shown in red, while fits using the function discussed in the text are plotted in blue. The two separate contributions to the fit arising from (i) Coulomb explosion of bound CH_3I molecules and (ii) Coulomb explosion following charge transfer between recently dissociated fragments are plotted in magenta and turquoise, respectively.

offset time than predicted. While this may hint at some deviations between the true mechanism of the charge transfer and the very simple model used here, it should also be noted that the total ion counts in this channel, and the quality of the fit, are relatively low. On this point, future similar experiments with a greater FEL intensity to probe the charge transfer from higher iodine charge states in this system would likely be of great interest.

Charge transfer involving multiply charged iodine atoms shortly after neutral dissociation should give rise to a delay-dependent Coulomb explosion channel. For example, for a charge transfer from a dissociated I^{n+}, this would result in high KE $I^{(n-1)+}$ and CH_3^+ ions. However, this feature, which would be most intense shortly after time-zero, is likely to overlap energetically with Coulomb explosion of undissociated parent molecules to $I^{(n-1)+}$ and CH_3^+ directly. To our best knowledge, such a feature has not been observed in previous experiments. However, in examining the time-dependence of the high KE channel in the I^{2+} and I^{3+} ions in particular, a small enhancement shortly after t_0 is clear, superimposed on the expected exponential decay associated with parent depletion as a result of predissociation. It is worth noting that the observed delay-dependence was fairly consistent across the entire broad high KE feature in both these ions, and different contributions could not be separated by their kinetic energies. As a result, the delay dependence of the total yields of all ions within the broad high KE band is investigated, as plotted in figure 8.

To investigate the origin of this feature, the data were fitted to a simple model incorporating contributions from (i) Coulomb explosion of bound molecules and (ii) Coulomb explosion following charge transfer between recently dissociated fragments. The predissociation was again assumed to follow unimolecular kinetics (i.e. an exponential time dependence), and it was assumed that charge transfer would occur for a certain critical time, τ_{crit}, following dissociation. The overall fit function is then obtained by a summed weighting of the contributions from intact molecules and charge transfer pairs. As with previous fits, a Gaussian convolution is performed to account for the experimental time resolution. Due to the presence of two contributions with unknown relative weightings, certain parameters had to be fixed in order for fitting to be possible. This is not a problem, as some parameters can be used from the previously described fits of the low KE ion yields, namely, the predissociation time, τ_{r}, and the critical time, τ_{crit}. As the charge transfer signal seen in the I^{2+} is assumed to arise from charge transfer between neutral CH_3 and I^{3+}, the critical time of this process should be the same as the observed time shift in the yields of low KE I^{3+} ions. An analogous argument can be made for the signal in the I^{3+} ion arising from charge transfer from I^{4+}. Upon fixing the value of these parameters, the delay-dependence of the high KE features in the I^{2+} and I^{3+} ions can be reliably fitted, with the weightings of the two previously mentioned contributions left as the only remaining fit parameters. The resulting fits are displayed in figure 8 and it can be seen that this model, incorporating an over-the-barrier picture of the charge transfer, can qualitatively reproduce the behavior seen experimentally. The exact form of the charge transfer contribution to these transients is predominantly determined by the experimental time-resolution of the current work. Future work with improved time-resolution to directly probe the delay dependence of this charge transfer signature in finer detail would be of great interest.

3.4. Photofragment angular distributions

The time-integrated iodine ion images presented in figure 4 highlight the significant anisotropy of the low KE feature; with a concentration of signal perpendicular to the laser and FEL polarization axis. Analysis of the ion images as a function of pump–probe delay reveals variation in the degree of this anisotropy, which can be characterized through the anisotropy parameter β. For the case of single-photon dissociation of an unaligned target, the photofragment angular distributions adopt a form [65] $I(\theta) = (\sigma/4\pi)[1 + \beta P_2(\cos^2\theta)]$. Here, σ refers to the total absorption cross section, θ is the angle between the linear polarization and the photofragment velocity vectors, and $P_2(\cos^2\theta)$ is a Legendre polynomial of second order. Presented in figure 9 is the β parameter extracted from fits to the KE integrated I^{3+} images for the low KE feature. This analysis could not be performed as reliably on the I^{2+} images, due to a FEL only background feature which overlaps energetically with the pump–probe feature of interest. Re-binning of the data into significantly coarser delay bins than those shown in figure 6 was required for the angular analysis due to relatively low statistics for each image in the previous

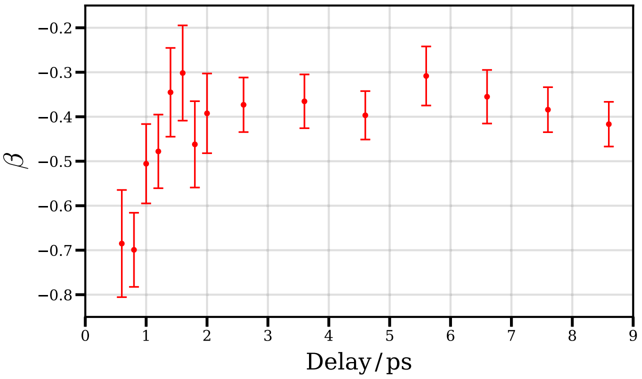

Figure 9. Photofragment anisotropy parameter β extracted for the $I^*(^2P_{1/2})$ channel as a function of pump–probe delay for the I^{3+} fragment. Error bars represent statistical errors of the fitted parameter. A discussion of the fitting methodology is presented in the main text.

binning. We note that, unlike the time-dependent KE analysis, the image analysis was performed on the central slice(s) of the Newton sphere associated with a particular iodine fragment rather than the 3D distribution or crushed images which require subsequent Abel inversion. This choice is motivated by the reduction in achievable angular resolution for time bins away from the central slice, due to the time resolution of the PImMS camera.

In the limit of a prompt dissociation process, the perpendicular nature of the $X \rightarrow B$ transition should give rise to a photofragment angular distribution with $\beta = -1$. Deviation from this expected value can arise from molecular rotation occurring on a comparable time scale to the dissociation process [66]. This is expected for the B-state predissociation in CH_3I where, slow (picosecond) crossing onto the A-band surface occurs, followed by sub-100 fs dissociation on the latter surface. Figure 9 reveals a value of $\beta = -0.7$ observed within the first few 100 femtoseconds, which decays towards approximately $= -0.4$ within 2 ps. The time-dependence of the extracted β parameter qualitatively matches the trend observed by Gitzinger *et al* where high degrees of anisotropy, close to $\beta = -1$, are observed at early pump–probe delays and an asymptotic value is reached with a few picoseconds [21]. There are, however, numerous subtle differences between the two measurements due to the temperature of the CH_3I sample. Despite the sample undergoing some degree of rotational cooling via the supersonic expansion, the rotational temperature of the sample needs to be considered as this corresponds to the rotational energy that causes the CH_3I axis distribution to evolve from the aligned distribution created by the pump pulses. A detailed discussion of the deviation of the asymptotic value of the iodine fragment angular distribution from the limiting case of $\beta = -1$ is provided in reference [24]. The authors highlight that asymptotic values closer to isotropic are reached for warmer targets and, therefore, variation between molecular beam expansion conditions (continuous versus pulsed jet, seeded versus non-seeded, etc) can give rise to differing values. A value of $\beta = -0.549 \pm 0.005$ was reported at a time delay of 8 ps, which is slightly higher than the asymptotic values of $\beta = -0.50 \pm 0.07$ reported in a previous study [21]. This small deviation is assigned to the use of a continuous versus a pulsed molecular beam source in the two studies, respectively. Unlike the previous results, where rare gas seeded expansions were used, our apparatus employed a neat expansion of CH_3I, which certainly correlates with a substantially higher rotational temperature. This assertion is in keeping with our asymptotic β of ~ -0.4. Finally, we note that recent nanosecond REMPI experiments from Xu and Pratt report a β value of -0.33 ± 0.01 for the $I^*(^2P_{1/2}) + CH_3$ channel after excitation to the 0^0_0 state of the B-band [25].

4. Conclusions

Results for a time-resolved imaging experiment investigating the predissociation and charge transfer dynamics in CH_3I using femtosecond XUV pulses at an FEL were presented. Excitation at 201.2 nm to the band origin of the B-state results in a predissociation process involving non-adiabatic coupling to the lower-lying strongly dissociative A-band. At our employed FEL photon energy of 95 eV, the ensuing C–I bond cleavage is probed in a site-specific manner due to the high absorption cross section of the iodine atom at this energy. In accord with several previous experimental [21, 24] as well as theoretical studies [3], a quantum yield close to one for the $I^*(^2P_{1/2}) + CH_3$ dissociation channel is observed. An appearance time of 1.53 ± 0.02 ps is reported for the iodine fragment, which was found to be largely invariant with respect to charge state, within our experimental uncertainty. Analysis of the onset time for each charge state, however, highlighted significant changes; with the lower charge states (e.g. I^{2+}) being produced at earlier times compared to higher ones (e.g. I^{6+}). This observation, similar to our previous work [9, 11], can be attributed to a charge transfer process occurring at smaller internuclear distances before the I and CH_3 cofragments have separated. Excellent agreement was found between the extracted time offsets as a function of charge state and estimates determined using a classical over-the-barrier model. Unlike previous studies, a slight enhancement in the yield of high KE I^{n+} ($n = 2$–3) ions shortly after time-zero was observed. This feature was assigned to Coulomb explosion as a result of charge transfer involving recently dissociated iodine atoms, following their multiple ionization by the XUV pulse. The delay-dependence of this feature could be broadly understood, again using a simple over-the-barrier model of the charge transfer. However, future studies employing shorter duration UV pulses, coupled with higher statistics and covariance analysis may be able to probe this feature and the underlying charge transfer dynamics far more intricately.

By exploiting the multimass time-stamping capabilities of the PImMS camera, the three-dimensional momentum of all iodine charge states could be recorded simultaneously. This resulted in significantly higher data rates, compared to conventional sliced imaging approaches, and circumvented the need for inversion techniques to reconstruct the full 3D data from a 2D crushed image, which typically introduce noise. The data presented here constitutes 3 h of experimental time at 10 Hz and highlights the applicability of our imaging approach to both time-pressured and parameter varying experiments, such as those conducted at FEL facilities. Sliced images were, however, utilized to investigate the photofragment angular distributions for the I$^*(^2P_{1/2})$ + CH_3 dissociation channel. A strong anisotropy perpendicular to the laser polarization is observed at short pump–probe delays, which becomes more isotropic due to rotation of the parent molecule prior to dissociation, a conclusion in accord with previous works [21, 24]. We note that our three-dimensional imaging approach could be readily extended to photofragment angular distributions by utilizing a faster time-stamping camera technology and/or correlation analysis with the ToF traces recorded from the MCP directly. Optimization of these imaging conditions will permit a new class of experiments to be performed that exploit, for example, complex polarization geometries and three-dimensional covariance imaging [67].

Acknowledgments

This research was carried out at FLASH-BL1 at DESY, a member of the Helmholtz Association (HGF). The research was further supported by the project CALIPSOplus under the Grant Agreement 730872 from the EU Framework Programme for Research and Innovation HORIZON 2020. The authors gratefully acknowledge the work of the scientific and technical teams at FLASH. We acknowledge the Max Planck Society for funding the development and the initial operation of the CAMP end-station within the Max Planck Advanced Study Group at CFEL and for providing this equipment for CAMP@FLASH. The installation of CAMP@FLASH was partially funded by the BMBF Grants 05K10KT2, 05K13KT2, 05K16KT3 and 05K10KTB from FSP-302. The authors are additionally thankful for support from the following funding bodies: the UK EPSRC (M Bu—EP/S028617/1; M Br and CV—EP/L005913/1); the Chemical Sciences, Geosciences, and Biosciences Division, Office of Basic Energy Sciences, Office of Science, US Department of Energy, Grant No. DE-FG02-86ER13491 (FZ and DR) and DE-SC0019451 (KB); the Helmholtz Initiative and Networking Fund through the Young Investigator Groups Program (SB); the Swedish Research Council and the Swedish Foundation for Strategic Research (JP and PJ) and; the National Science Foundation (RF, AH and PHB). The authors are grateful to Aleksey Alekseyev for generously providing the potential energy curves used to generate figure 1.

ORCID iDs

Ruaridh Forbes https://orcid.org/0000-0003-2097-5991
Rebecca Boll https://orcid.org/0000-0001-6286-4064
Bastian Manschwetus https://orcid.org/0000-0001-6165-9560
Claire Vallance https://orcid.org/0000-0003-3880-8614
Daniel Rolles https://orcid.org/0000-0002-3965-3477
Michael Burt https://orcid.org/0000-0002-7317-8649

References

[1] Ogorzalek Loo R, Haerri H, Hall G E and Houston P L 1989 Methyl rotation, vibration, and alignment from a multiphoton ionization study of the 266 nm photodissociation of methyl iodide *J. Chem. Phys.* **90** 4222

[2] Eppink A T J B and Parker D H 1999 Energy partitioning following photodissociation of methyl iodide in the A band: a velocity mapping study *J. Chem. Phys.* **110** 832

[3] Alekseyev A B, Liebermann H-P, Buenker R J and Yurchenko S N 2007 An *ab initio* study of the CH_3I photodissociation. I. Potential energy surfaces *J. Chem. Phys.* **126** 234102

[4] Alekseyev A B, Liebermann H-P and Buenker R J 2011 *Ab initio* configuration interaction study of the B- and C-band photodissociation of methyl iodide *J. Chem. Phys.* **134** 044303

[5] de Nalda R, Izquierdo J G, Durá J and Bañares L 2007 Femtosecond multichannel photodissociation dynamics of CH_3I from the A band by velocity map imaging *J. Chem. Phys.* **126** 021101

[6] de Nalda R, Durá J, García-Vela A, Izquierdo J G, González-Vázquez J and Bañares L 2008 A detailed experimental and theoretical study of the femtosecond A-band photodissociation of CH_3I *J. Chem. Phys.* **128** 244309

[7] García-Vela A, de Nalda R, Durá J, González-Vázquez J and Bañares L 2011 A 4D wave packet study of the CH_3I photodissociation in the A-band. Comparison with femtosecond velocity map imaging experiments *J. Chem. Phys.* **135** 154306

[8] Zhong D and Zewail A H 1998 Femtosecond real-time probing of reactions. 23. studies of temporal, velocity, angular, and state dynamics from transition states to final products by femtosecond-resolved mass spectrometry *J. Phys. Chem.* A **102** 4031

[9] Erk B *et al* 2014 Imaging charge transfer in iodomethane upon x-ray photoabsorption *Science* **345** 288

[10] Brauße F *et al* 2018 Time-resolved inner-shell photoelectron spectroscopy: from a bound molecule to an isolated atom *Phys. Rev.* A **97** 043429

[11] Amini K *et al* 2018 Photodissociation of aligned CH_3I and $C_6H_3F_2I$ molecules probed with time-resolved Coulomb explosion imaging by site-selective extreme ultraviolet ionization *Struct. Dyn.* **5** 014301

[12] Boll R *et al* 2016 Charge transfer in dissociating iodomethane and fluoromethane molecules ionized by intense femtosecond x-ray pulses *Struct. Dyn.* **3** 043207

[13] Attar A R, Bhattacherjee A and Leone S R 2015 Direct observation of the transition-state region in the photodissociation of CH_3I by femtosecond extreme ultraviolet transient absorption spectroscopy *J. Phys. Chem. Lett.* **6** 5072

[14] Drescher L, Galbraith M C E, Reitsma G, Dura J, Zhavoronkov N, Patchkovskii S, Vrakking M J J and Mikosch J 2016 Communication: XUV transient absorption spectroscopy of iodomethane and iodobenzene photodissociation *J. Chem. Phys.* **145** 011101

[15] Olney T N, Cooper G and Brion C 1998 Quantitative studies of the photoabsorption (4.5–488 eV) and photoionization (9–59.5 eV) of methyl iodide using dipole electron impact techniques *Chem. Phys.* **232** 211

[16] Forbes R *et al* 2020 Photoionization of the I 4d and valence orbitals of methyl iodide *J. Phys.* B **53** 155101

[17] Eden S, Limão-Vieira P, Hoffmann S V and Mason N J 2007 VUV spectroscopy of CH_3Cl and CH_3I *Chem. Phys.* **331** 232

[18] Dobber M R, Buma W J and de Lange C A 1993 Resonance enhanced multiphoton ionization photoelectron spectroscopy on nanosecond and picosecond time scales of Rydberg states of methyl iodide *J. Chem. Phys.* **99** 836

[19] Owrutsky J and Baronavski A 1994 Lifetimes of the $\tilde{B}$ state of CH_3I and CD_3I using femtosecond resonance enhanced multiphoton ionization *Chem. Phys. Lett.* **222** 335

[20] Baronavski A P and Owrutsky J C 1998 Vibronic dependence of the $\tilde{B}$ state lifetimes of CH_3I and CD_3I using femtosecond photoionization spectroscopy *J. Chem. Phys.* **108** 3445

[21] Gitzinger G, Corrales M E, Loriot V, Amaral G A, de Nalda R and Bañares L 2010 A femtosecond velocity map imaging study on B-band predissociation in CH_3I. I. The band origin *J. Chem. Phys.* **132** 234313

[22] González M G, Rodríguez J D, Rubio-Lago L and Bañares L 2011 Communication: first observation of ground state $I(^2P_{3/2})$ atoms from the CH_3I photodissociation in the B-band *J. Chem. Phys.* **135** 021102

[23] Gitzinger G, Corrales M E, Loriot V, de Nalda R and Bañares L 2012 A femtosecond velocity map imaging study on B-band predissociation in CH_3I. II. The 2_1^0 and 3_1^0 vibronic levels *J. Chem. Phys.* **136** 074303

[24] Thiré N, Cireasa R, Staedter D, Blanchet V and Pratt S T 2011 Time-resolved predissociation of the vibrationless level of the B state of CH_3I *Phys. Chem. Chem. Phys.* **13** 18485

[25] Xu H and Pratt S T 2015 Photodissociation of methyl iodide via selected vibrational levels of the $\tilde{B}(^2E_{3/2})$6s Rydberg state *J. Phys. Chem.* A **119** 7548

[26] Nomerotski A *et al* 2011 Pixel imaging mass spectrometry with fast silicon detectors *Nucl. Instrum. Methods* A **633** S243

[27] John J J *et al* 2012 PImMS, a fast event-triggered monolithic pixel detector with storage of multiple timestamps *J. Instrum.* **7** C08001

[28] Ryufuku H, Sasaki K and Watanabe T 1980 Oscillatory behavior of charge transfer cross sections as a function of the charge of projectiles in low-energy collisions *Phys. Rev.* A **21** 745

[29] Erk B *et al* 2018 CAMP@FLASH: an end-station for imaging, electron- and ion-spectroscopy, and pump–probe experiments at the FLASH free-electron laser *J. Synchrotron Radiat.* **25** 1529

[30] Ackermann W, Asova G, Ayvazyan V *et al* 2007 Operation of a free electron laser in the wavelength range from the extreme ultraviolet to the water window *Nat. Photon.* **1** 336

[31] Redlin H, Al-Shemmary A, Azima A, Stojanovic N, Tavella F, Will I and Düsterer S 2011 The FLASH pump–probe laser system: setup, characterization and optical beamlines *Nucl. Instrum. Methods* A **635** S88

[32] Rolles D, Boll R, Erk B, Rompotis D and Manschwetus B 2018 An experimental protocol for femtosecond NIR/UV - XUV pump–probe experiments with free-electron lasers *J. Vis. Exp.* e57055

[33] Krikunova M *et al* 2009 Time-resolved ion spectrometry on xenon with the jitter-compensated soft x-ray pulses of a free-electron laser *New J. Phys.* **11** 123019

[34] Uiberacker M *et al* 2007 Attosecond real-time observation of electron tunnelling in atoms *Nature* **446** 627

[35] Garcia G A, Nahon L and Powis I 2004 Two-dimensional charged particle image inversion using a polar basis function expansion *Rev. Sci. Instrum.* **75** 4989

[36] Düsterer S *et al* 2014 Development of experimental techniques for the characterization of ultrashort photon pulses of extreme ultraviolet free-electron lasers *Phys. Rev. Spec. Top. Accel. Beams* **17** 120702

[37] Eppink A T J B and Parker D H 1997 Velocity map imaging of ions and electrons using electrostatic lenses: application in photoelectron and photofragment ion imaging of molecular oxygen *Rev. Sci. Instrum.* **68** 3477

[38] Slater C S *et al* 2015 Coulomb-explosion imaging using a pixel-imaging mass-spectrometry camera *Phys. Rev.* A **91** 053424

[39] Allum F *et al* 2018 Coulomb explosion imaging of CH_3I and CH_2ClI photodissociation dynamics *J. Chem. Phys.* **149** 204313

[40] Slater C S *et al* 2014 Covariance imaging experiments using a pixel-imaging mass-spectrometry camera *Phys. Rev.* A **89** 011401

[41] Manura D and Dahl D 2006 *SIMION (R) 8.0*

[42] Savelyev E *et al* 2017 Jitter-correction for IR/UV-XUV pump–probe experiments at the FLASH free-electron laser *New J. Phys.* **19** 043009

[43] Tiedtke K *et al* 2008 Gas detectors for x-ray lasers *J. Appl. Phys.* **103** 094511

[44] Löhl F *et al* 2010 Electron bunch timing with femtosecond precision in a superconducting free-electron laser *Phys. Rev. Lett.* **104** 144801

[45] Saito N and Suzuki I H 1992 Multiple photoionization in Ne, Ar, Kr and Xe from 44 to 1300 eV *Int. J. Mass Spectrom.* **115** 157

[46] Dasch C J 1992 One-dimensional tomography: a comparison of Abel, onion-peeling, and filtered backprojection methods *Appl. Opt.* **31** 1146

[47] Vrakking M J 2001 An iterative procedure for the inversion of two-dimensional ion/photoelectron imaging experiments *Rev. Sci. Instrum.* **72** 4084

[48] Zhao K, Colvin T, Hill W T and Zhang G 2002 Deconvolving two-dimensional images of three-dimensional momentum trajectories *Rev. Sci. Instrum.* **73** 3044

[49] Dribinski V, Ossadtchi A, Mandelshtam V A and Reisler H 2002 Reconstruction of Abel-transformable images: the Gaussian basis-set expansion Abel transform method *Rev. Sci. Instrum.* **73** 2634

[50] Roberts G M, Nixon J L, Lecointre J, Wrede E and Verlet J R 2009 Toward real-time charged-particle image reconstruction using polar onion-peeling *Rev. Sci. Instrum.* **80** 053104

[51] Dick B 2014 Inverting ion images without Abel inversion: maximum entropy reconstruction of velocity maps *Phys. Chem. Chem. Phys.* **16** 570

[52] Gebhardt C R, Rakitzis T P, Samartzis P C, Ladopoulos V and Kitsopoulos T N 2001 Slice imaging: a new approach to ion imaging and velocity mapping *Rev. Sci. Instrum.* **72** 3848

[53] Townsend D, Minitti M P and Suits A G 2003 Direct current slice imaging *Rev. Sci. Instrum.* **74** 2530

[54] Lin J J, Zhou J, Shiu W and Liu K 2003 Application of time-sliced ion velocity imaging to crossed molecular beam experiments *Rev. Sci. Instrum.* **74** 2495

[55] Ullrich J, Moshammer R, Dorn A, Dörner R, Schmidt L P H and Schmidt-Böcking H 2003 Recoil-ion and electron momentum spectroscopy: reaction-microscopes *Rep. Prog. Phys.* **66** 1463

[56] Schmid G *et al* 2019 Reaction microscope endstation at FLASH2 *J. Synchrotron Radiat.* **26** 854

[57] Fisher-Levine M and Nomerotski A TimepixCam: a fast optical imager with time-stamping *J. Instrum.* **11** C03016

[58] Nomerotski A 2019 Imaging and time stamping of photons with nanosecond resolution in timepix based optical cameras *Nucl. Instrum. Methods Phys. Res. Sect. A Accel. Spectrom. Detect. Assoc. Equip.* **937** 26

[59] Amini K, Blake S, Brouard M, Burt M B, Halford E, Lauer A, Slater C S, Lee J W L and Vallance C 2015 Three-dimensional imaging of carbonyl sulfide and ethyl iodide photodissociation using the pixel imaging mass spectrometry camera *Rev. Sci. Instrum.* **86** 103113

[60] Fisher-Levine M, Boll R, Ziaee F, Bomme C, Erk B, Rompotis D, Marchenko T, Nomerotski A and Rolles D 2018 Time-resolved ion imaging at free-electron lasers using timepix-Cam *J. Synchrotron Radiat.* **25** 336

[61] Champenois E 2017 cPBASEX https://github.com/e-champenois/CPBASEX

[62] Zhao A *et al* 2017 Coincidence velocity map imaging using Tpx3Cam, a time stamping optical camera with 1.5 ns timing resolution *Rev. Sci. Instrum.* **88** 113104

[63] Stapelfeldt H, Constant E and Corkum P B 1995 Wave packet structure and dynamics measured by Coulomb explosion *Phys. Rev. Lett.* **74** 3780

[64] Ding X *et al* 2019 Threshold photodissociation dynamics of NO_2 studied by time-resolved cold target recoil ion momentum spectroscopy *J. Chem. Phys.* **151** 174301

[65] Yang C N 1948 On the angular distribution in nuclear reactions and coincidence measurements *Phys. Rev.* **74** 764

[66] Yang S and Bersohn R 1974 Theory of the angular distribution of molecular photofragments *J. Chem. Phys.* **61** 4400

[67] Lee J W L, Koeckert H, Heathcote D, Popat D, Chapman R T, Karras G, Majchrzak P, Springate E and Vallance C 2020 Three-dimensional imaging probe of molecular structure and dynamics on the ultrafast timescale *Commun. Chem.* **3** 72